International Journal of Heat and Mass Transfer 266 (2026) 128840

Contents lists available at ScienceDirect

International Journal of Heat and Mass Transfer

journal homepage: www.elsevier.com/locate/hmt

Effects of inlet temperature and pressure in sCO_2 heat transfer in a 1 mm diameter horizontal tube

Camila Pedano-Medina [a,b,c,*], Paolo Petagna [a], Susanne Gleissle [b]

[a] CERN (European Organization for Nuclear Research), Esplanade des Particules 1, Geneva, 1211, Geneva, Switzerland
[b] Offenburg University of Applied Sciences, Badstrasse 24, Offenburg, 77652, Baden-Wurttemberg, Germany
[c] Karlsruhe Institute of Technology - Department of Chemical and Process Engineering, Engler-Bunte-Ring 1b, Karlsruhe, 76131, Baden-Wurttemberg, Germany

ARTICLE INFO

Keywords:
Carbon dioxide
Supercritical
Detector cooling
Heat transfer
Pressure drop
Experimental

ABSTRACT

Supercritical CO_2 (sCO_2) is of high interest for compact cooling applications, yet local heat transfer data in millimetric scale horizontal tubes under electronics-relevant conditions remain scarce. This work reports local heat transfer coefficients, pressure drops and temperature-inlet-to-outlet values for CO_2 at inlet pressures from 7.5 to 8.5 MPa flowing in a 1 mm horizontal stainless-steel tube with $G = 2130\ \mathrm{kg\,m^{-2}\,s^{-1}}$ ($\dot{m} \approx 1.8\ \mathrm{g\,s^{-1}}$) and uniform Joule heating over $L_h = 0.903$ m at $q = 35\ \mathrm{kW\,m^{-2}}$. A calorimetric data reduction based on inlet and outlet conditions is combined with an axial enthalpy integration to express results as a function of bulk enthalpy, thus enabling consistent comparison across inlet temperatures.

The obtained heat transfer coefficients span from 10 to 60 $\mathrm{kW\,m^{-2}\,K^{-1}}$ and show a systematic dependence on inlet temperature and pressure through the pseudo-critical region. When the fluid near the wall crosses the pseudo-critical point, a first enhancement is observed, associated with the sharp increase in c_p, causing the collapse of $(T_w - T_b)$. The overall pressure drop increases steeply as inlet conditions approach the pseudo-critical temperature, whereas the inlet-to-outlet temperature rise decreases and tends to plateau, highlighting the thermal–hydraulic trade-off in this regime. Additionally, comparison with Petukhov (P) and Krasnoshchekov–Kuraeva–Protopopov (KKP) correlations shows that KKP captures about 85% of data within ±20%, while P overpredicts at high heat transfer coefficients due to the lack of consideration of strong radial property variations.

These results provide a benchmark dataset of high Reynolds numbers, low heat flux sCO_2 heat transfer in 1 mm horizontal channels and show an improved performance of sCO_2 as a local single-phase refrigerant, making it a promising alternative for detector and electronics cooling at warm operating temperatures above 31 °C.

1. Introduction

Research on heat transfer with supercritical fluids dates back to the 1930s with the first studies on free convection near the critical point [1]. In the 1970s, applications were diverse: near-critical helium for cooling superconducting magnet coils, supercritical hydrogen as a rocket fuel, supercritical water in power generation, and methane as both coolant and fuel for supersonic transport [2]. Today, sCO_2 is considered the reference fluid for studying supercritical heat transfer, owing to its relatively low critical point, which makes laboratory experiments accessible. Consequently, carbon dioxide has been widely employed as a modelling fluid throughout the last century, particularly in nuclear reactor research [3]. More recently, interest in sCO_2 has started to expand to electronics cooling and other applications where high heat fluxes must be managed in compact geometries [4]. Despite this growing interest, there has not yet been experimental work explicitly dedicated to sCO_2 as a coolant for electronics in small pipes.

Electronics cooling places strict demands on temperature stability, heat flux dissipation and compactness, which in turn set tight constraints on the thermo-physical and hydraulic behaviour of the coolant.

Single-phase liquid cooling is typically the first choice for the thermal management of electronics whenever heat removal by forced air convection is not enough. This is mainly due to the design simplicity of single-phase cooling systems and to the stable and predictable thermo-hydraulic behaviour of single-phase flows in ducts. However, when the dissipated power density becomes high and space limitations impose the use of small diameter pipes, single-phase liquid cooling becomes insufficient, due to the large thermal gradients involved, or to the high

* Corresponding author at: CERN (European Organization for Nuclear Research), Esplanade des Particules 1, Geneva, 1211, Geneva, Switzerland.
E-mail address: camila.pedano@cern.ch (C. Pedano-Medina).

https://doi.org/10.1016/j.ijheatmasstransfer.2026.128840
Received 5 February 2026; Received in revised form 28 March 2026; Accepted 8 April 2026
Available online 25 April 2026

flow speeds required to limit the temperature increase, involving high pumping powers and risks of erosion of the pipe walls.

The management of high thermal loads in confined spaces is typical of many electronics application cases. For particle detector electronics, CO_2 evaporation cooling in mini- and micro-channels has been used for over a decade [5]. Boiling flows are highly effective because they dissipate large amounts of heat with limited temperature increase, due to the latent heat of evaporation. Furthermore, since temperature variations are only due to the pressure drop along the cooling path, they exhibit only minimal changes in bulk temperature enabling nearly isothermal operation. Finally, the heat transfer coefficients achieved by flows boiling in small diameter pipes are much larger than those achievable by single-phase flows under comparable conditions.

In contrast, two-phase cooling systems require more complex systems than their single-phase counterparts, especially when manifolds are required; and the prediction of thermo-hydraulic behaviour of boiling flows in ducts relies on semi-empirical correlations of very limited general validity.

Supercritical fluids lack a latent heat of vaporization, since distinct liquid and vapour phases no longer exist above the critical point. Instead, in a nearly isobaric process, a supercritical fluid undergoes a continuous transition from a liquid-like to a vapour-like state as temperature increases. This can offer many advantages related to the simplicity of working with a single phase, while offering a performance comparable to two-phase coolants.

A defining feature of supercritical fluids is the steep variation of physical properties at the vicinity of the critical point. This behaviour is illustrated in Fig. 1, which displays the variation of density, isobaric heat capacity, viscosity and thermal conductivity of CO_2 across the critical region. Enthalpy was chosen as the independent variable to define the thermodynamic state of the fluid. In heated flows, particularly near the pseudo-critical region, enthalpy provides a more practical and physically meaningful axis than temperature, because it directly reflects the progression of the energy balance along the channel. The high specific heat capacity near the pseudo-critical point implies that the fluid can absorb significant thermal loads with only a modest temperature rise, suggesting the possibility of designing cooling systems that approach isothermal operation even without phase change. At the same time, the density and viscosity variation showcase the liquid-like to vapour-like transition and affect the velocity profile and turbulence characteristics in such systems. Such variations provide the potentiality to achieve very high heat transfer coefficients while keeping at low values the pressure drop along the cooling pipes.

The advantage of using sCO_2 over other refrigerants depends naturally on the specific application conditions. Nevertheless, carbon dioxide presents a fundamental benefit compared with synthetic refrigerants such as fluorocarbons: it exists naturally in the environment. As the European Commission bans fluorocarbons and other high-GWP refrigerants [7], the remaining long-term options are the so-called ‘green’ fluids. Other natural coolants include ammonia, water and certain hydrocarbons, each with their own advantages and limitations depending on the boundary conditions of the system.

For electronics cooling, hydrocarbons can only find very limited applications due to their flammability. Water is widely used as a coolant because of its exceptionally high specific heat capacity. However, in conventional commercial systems water operates as a low-pressure refrigerant, and pressure drop becomes a limiting factor—particularly in the small-diameter channels characteristic of compact electronics cooling. In addition, water is electrically conductive and therefore presents a risk when circulated near sensitive electronic components.

This study provides a dedicated experimental dataset of sCO_2 heat transfer behaviour under operational conditions representative of electronics cooling applications. In particular, typical working parameters for one cooling circuit segment of a silicon detector in the LHC at CERN are selected for the analysis, in this case meaning a power density of 35 $kW\,m^{-2}$.

2. Literature review and scope of the present work

Previous studies have highlighted the potentially high heat transfer coefficients attainable with sCO_2 [8,9]. However, the open literature shows rather inconsistent results and diverse conclusions are extracted from different studies. As already emphasized by Hendricks [2], near-critical heat transfer data can differ significantly between test rigs, implying that system and geometry effects play a non-negligible role in the inconsistencies observed across studies. These inconsistencies may also be enhanced due to several factors, many of which are discussed in this work.

Although heat transfer studies with supercritical CO_2 are abundant, only a limited number provide data in the small-diameter range relevant to electronics cooling. Wang et al. [9] reported the first *local*[1] heat transfer coefficients in tubes below 2 mm, with diameters of 0.5, 0.75 and 1 mm, and observed values between 1.6–3.3 kW/m^2 K under moderate mass fluxes. Their comparison with existing correlations revealed significant discrepancies, reflecting the limited predictive capability of models developed for larger diameters or vertical pipes. Guo et al. [10] evaluated *average* heat transfer coefficients in a 2 mm horizontal tube and highlighted the role of buoyancy through top–bottom temperature differences, again noting that correlations failed to reproduce their trends (and subsequently developing their own).

Earlier work by Liao and Zhao [11] already demonstrated strong effects of flow orientation and diameter in their *average* heat transfer coefficients, showing that their 0.7 mm and 1.4 mm pipes were strongly affected by buoyancy effects in conditions when the reduced pressure approached 1. The effect of inlet temperature was not thoroughly considered in the literature until Kline et al. [12] presented that local wall temperature profiles changed depending on the inlet temperature at otherwise equal system conditions. More recently, Theologou et al. [8] showed that the inlet temperature controls both the magnitude and axial development of local heat transfer coefficients in 4 mm and 8 mm tubes.

Across these studies, a consistent picture emerges: the qualitative behaviour of heat transfer is dictated by the strong near-critical variation of thermophysical properties. Classical work by Yamagata et al. [13] and Jackson [14] showed that the steep rise in heat capacity near the pseudo-critical point enhances heat transfer in the absence of buoyancy, while density gradients may introduce additional acceleration or stratification effects. However, the combined effect of tube diameter, inlet temperature and buoyancy remains only partially explored, and data for 1 mm horizontal tubes at high Reynolds number are essentially absent. The lack of local measurements in small horizontal channels limits the development and validation of predictive models.

Other recent works address heat transfer properties of CO_2 in compact geometries. However, they either focus on measurements of applied heat exchanger performances [15], or treat the subject from a purely numerical point of view [16,17]. Additionally, no direct reports of temperature increase along the pipe, nor pressure drop, are easily accessible in the open literature.

The present study contributes to filling this gap by providing local heat transfer coefficients in a 1 mm tube at high mass flux and low heat flux; conditions typical of detector or electronics cooling, but scarcely documented in the literature. Smaller diameters reduce stratification effects and also limit the space available for radial property gradients to develop, allowing more uniform flow characteristics in the radial axis. This could potentially mitigate buoyancy effects in supercritical heat transfer, which heavily impacts the early deterioration of heat transfer seen in larger pipes [18]. This is, for instance, shown in Fig. 9, discussed in a further section.

[1] In this context, the term *local* refers to the rate of heat transfer between the fluid and the surface at a specific location along a flow path.

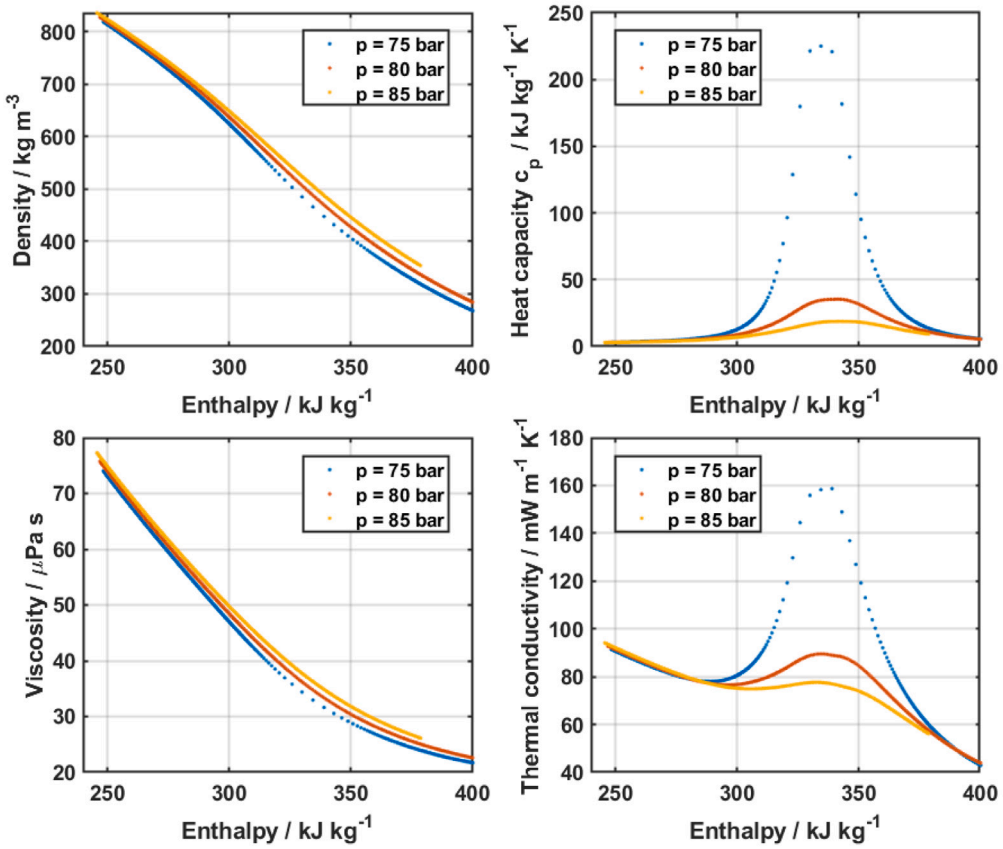

Fig. 1. Thermophysical properties of CO_2 as a function of enthalpy at different pressures across the critical region: density (top left), isobaric heat capacity (top right), viscosity (bottom left), and thermal conductivity (bottom right).
Source: Properties extracted from [6].

Furthermore, essential details such as the purity of the CO_2 used have not always been reported in the literature, making comparison and reproducibility difficult. The omission of such parameters has led to a lack of essential information for the reader and may partly explain the variability observed across datasets. Kurganov et al. [19] showed the effect of different impurities in the estimation of the physical properties of a supercritical fluid and emphasized that even small increases of air in the mixture decreased the temperature of the specific heat maximum at a given pressure. In general, carbon dioxide bottles can be found with different *qualities*,[2] where the term reflects the amount of impurities in the fluid. For supercritical applications, carbon dioxide with 99.998% mass purity is recommended (the rest is air, mainly nitrogen). Fig. 2 shows the variation of the isobaric heat capacity with temperature at different system pressures and different mixture concentrations. It can be seen from the diagram that two phenomena are encountered at different carbon dioxide qualities: the temperature at which the maximum c_p is achieved (pseudo-critical temperature) is displaced towards the left; meaning that the pseudo-critical temperature is reduced for a given pressure when using 99.5% carbon dioxide (the standard quality used in industrial and medical applications) with respect to 99.998%. Additionally, the c_p maxima decreases with lower concentration of carbon dioxide for the two pressures shown: around 15% at 8 MPa, and less than 5% at 9 MPa. In this work, the physical properties used for all

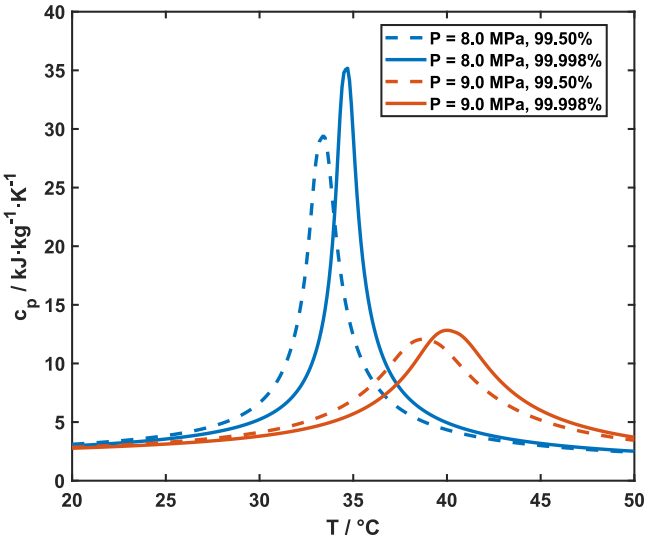

Fig. 2. Variation of the isobaric heat capacity of carbon dioxide at two different system pressures and purities with temperature.

calculations are obtained using the pre-defined mixture 'co2.q48' from REFPROP [6], which already considers the purity 99.998%.

This study provides novel results of the heat transfer coefficients and pressure drops obtained with carbon dioxide (99.998% purity) at 7.5, 8 and 8.5 MPa flowing horizontally in a 1 mm pipe with a mass flux

[2] How the purity of the fluid is indicated depends on the manufacturer. A common method is to report a quality of two digits where the first digit represents the number of 9s and the second digit the number after the last 9. For example, CO_2 48 or CO_2 4.8 is carbon dioxide with 99.998% carbon dioxide purity.

of 2130 kg/m^2 s (1.8 g/s mass flow rate) with a heat flux 35 kW/m^2 (100 W over a length of 0.9 m).

3. Experimental setup

The test rig is depicted in Fig. 3 and consists mainly of two main parts: fluid conditioning and test section. The fluid conditioning consists of a pumped loop where pressurized carbon dioxide (by means of AC-101) is flowed with a liquid pump (LP-101). The fluid is then filtered to remove any debris and the flow is regulated with a bypass valve (MV-105) and measured in FT-101. After this, the fluid is heated to the desired temperature with an electric heater (EH-101). Downstream of the electric heater, the fluid is sent to the second stage, the test section. In this stage, the fluid is sent to the capillary-sized pipe in order to determine heat transfer coefficients and pressure drops along the test section, which is inside the dashed lines in Fig. 3, as well as further detailed in the sketch shown in Fig. 4.

Power is supplied to the test section by means of Joule heating. In the sketch, three rectangular blocks show the attachment points of the resistive heater. By adding a positive electrode in the centre and two negative electrodes on the sides, the power provided is contained within the powered length. A distance of more than 50 diameters was left before the start of heating.[3] The assumptions of developed flow at such distance remain an assumption that, although is valid at subcooled conditions and when sufficiently far from the pseudo-critical point, remains a topic that deserves further study [8].

In the sketch, circles represent the wall temperature measurement points: 10 in the heated zone and one in the adiabatic zone. These are coated in a small layer of electrical insulation, covered in thermal conductive paste and placed directly in contact with the wall of the test section. They are kept in place using steel-filled epoxy putty. Additionally, Table 2 collects all the information regarding the dimensions and accuracies relative to the test section and measurements, including sensor axial positions. The test section is fully contained in a insulated box.

For operation, the desired pressure can be set by allowing nitrogen in AC-101 with FR-101. Then, the pump rotation speed is regulated with a variable frequency drive. The mass flow can be then set using MV-105 and once this is stable, the EH-101 is regulated to provide carbon dioxide flow at the desired operating temperature. The Joule heating can be set by regulating the power in EH-102. Since an addition of power in any of the heaters will cause the pressure drop of the system to increase, the mass flow has to be adjusted every time the heaters are used. This is performed by an on-site operator, which constantly monitors the system with help of a dedicated software developed in LabVIEW, for which the code can be publicly accessed in the CO2-SASS Gitlab repository.

Steady state is considered when the fluctuation of the temperature and pressure signals falls below the accuracy level for at least 5 min. The data is recorded at a frequency of 1 Hz for 5 min.

A fully detailed description of the test rig, containing all relevant information (including its design, sensor placement, calibration, and uncertainty analysis) is provided in the open access Ref. [21].

4. Data reduction and uncertainty

4.1. Data reduction

The heat absorbed by the fluid is calculated *calorimetrically*[4] by means of the inlet and outlet pressure and temperature conditions, as well as the mass flow; with the energy balance shown in Eq. (1).

$$\dot{Q} = \dot{m}[h(T_{f,out}, p_{out}) - h(T_{f,in}, p_{in})] \tag{1}$$

To mitigate the high sensitivity of enthalpy to small temperature uncertainties near the pseudo-critical point, where calorimetric error can exceed 100% [8], the electrical power was simultaneously monitored. The electrical input was corrected by a factor of 0.972 to account for electrode contact resistance and voltage drop–by measuring the direct

Table 1
Correlations used for comparison with the experimental data.

Petukhov correlation (P) [22]

$$Nu = \frac{(\xi/8)\, Re\, Pr}{k + 12.7\sqrt{\xi/8}\,(Pr^{2/3} - 1)}$$

$$k = 1.07 + \frac{900}{Re} - \frac{0.63}{1 + 10Pr}, \qquad \xi = \left(1.82 \log_{10} Re - 1.64\right)^{-2}$$

Applicable to $Re = 10^4 - 10^5$ and $Pr = 0.5 - 200$.
The Gnielinski correlation [23] is a modified version of Petukhov correlation where $k = 1.07$.

Krasnoshchekov–Kuraeva–Protopopov (KKP) [24]

$$Nu = Nu_{\text{Gnielinski}} \left(\frac{\rho_w}{\rho_b}\right)^{0.3} \left(\frac{\bar{c}_p}{c_{p,b}}\right)^n$$

$$\bar{c}_p = \frac{h_w - h_b}{T_w - T_b}$$

$$n = \begin{cases} 0.4 & T_b < T_w < T_m \text{ and } 1.2\,T_m < T_b < T_w \\ 0.4 + 0.2\left(\frac{T_w}{T_m} - 1\right) & T_b < T_m < T_w \\ 0.4 + 0.2\left(\frac{T_w}{T_m} - 1\right)\left[1 - 5\left(\frac{T_b}{T_m} - 1\right)\right] & T_m < T_b < 1.2\,T_m,\ T_b < T_w \end{cases}$$

Applicable to:

$$1.01 \le \frac{P}{P_{cr}} \le 1.33, \qquad 0.6 \le \frac{T_b}{T_m} \le 1.2, \qquad 0.6 \le \frac{T_w}{T_m} \le 2.6, \tag{16}$$

$$2 \times 10^4 \le Re_b \le 8 \times 10^5, \qquad 0.85 \le Pr_b \le 55, \qquad 0.09 \le \frac{\rho_w}{\rho_b} \le 1.0, \tag{17}$$

$$0.02 \le \frac{c_{p,w}}{c_{p,b}} \le 4.0, \qquad 2.3 \times 10^4 \le q_w \le 2.6 \times 10^6 \text{ W/m}^2, \qquad \frac{l}{d} > 15 \tag{18}$$

Jackson and Hall (JH) correlation [25]

$$Nu_b = 0.0183\, Re_b^{0.82}\, Pr_b^{0.5} \left(\frac{\rho_w}{\rho_b}\right)^{0.3} \left(\frac{\bar{c}_p}{c_{p,b}}\right)^n$$

$$\bar{c}_p = \frac{h_w - h_b}{T_w - T_b}$$

$$n = \begin{cases} 0.4 & T_b < T_w < T_m \text{ and } 1.2\,T_m < T_b < T_w \\ 0.4 + 0.2\left(\frac{T_w}{T_m} - 1\right) & T_b < T_m < T_w \\ 0.4 + 0.2\left(\frac{T_w}{T_m} - 1\right)\left[1 - 5\left(\frac{T_b}{T_m} - 1\right)\right] & T_m < T_b < 1.2\,T_m,\ T_b < T_w \end{cases}$$

where T_b, T_{pc} and T_w are in K.
Applicable to:

$$8 \times 10^4 \le Re_b \le 5 \times 10^5, \qquad 0.85 \le \overline{Pr}_b \le 65, \qquad 0.90 \le \frac{\rho_w}{\rho_b} \le 1.0, \tag{19}$$

$$0.9 \le \frac{T_w}{T_{pc}} \le 2.5, \qquad 4.6 \times 10^4 \le q_w \le 2.6 \times 10^6 \text{ W/m}^2, \qquad \frac{x}{D} \ge 15 \tag{20}$$

Jackson–Fewster (JF) correlation [26]

$$Nu_b = 0.0183\, Re_b^{0.82}\, Pr_b^{0.5} \left(\frac{\rho_w}{\rho_b}\right)^{0.3}$$

Wang (W) correlation [9]

$$Nu_z = 0.225\, Re_{b,z}^{0.423}\, Pr_{b,z}^{0.229} \left(Bo^*_{b,z}\right)^{-0.156} (T^*)^{0.055} \left(\frac{\bar{c}_{p,z}}{c_{p,b,z}}\right)^{0.401}$$

$$\bar{c}_{p,z} = \frac{h_{w,z} - h_{b,z}}{T_{w,z} - T_{b,z}}, \qquad T^* = \frac{T_m - T_{b,\text{in}}}{T_{b,\text{out}} - T_{b,\text{in}}}$$

$$Bo^*_{b,z} = \frac{Gr_{b,z}}{Re^2_{b,z}}, \qquad Gr_{b,z} = \frac{\left(\rho_{w,z} - \rho_{b,z}\right) g\, \rho_{b,z}\, D^3_{s,i}}{\mu^2_{b,z}}$$

Applicable to: $0.5 \le D_{s,i} \le 1.0$ mm, $76.6 \le P_{\text{out}} \le 90.0$ bar, $30.8 \le T_{f,\text{in}} \le 37.3$ °C, $672 \le G \le 4810$ kg m^{-2} s^{-1}, $70.7 \le q'' \le 344.2$ kW m^{-2}.
Wang et al. [9] define the Richardson number as Bo^*.

Guo (G) correlation [10]

$$Nu_b = 0.114\, Re_b^{0.589}\, Pr_b^{0.465} \left(\frac{Gr}{Re_b^2}\right)^{-0.125} \left(\frac{\rho_w}{\rho_b}\right)^{0.240} \left(\frac{\bar{c}_p}{c_{p,b}}\right)^{0.096}$$

$$\bar{c}_p = \frac{h_w - h_b}{T_w - T_b}$$

Applicable to: $7.6 \le p \le 8.4$ MPa, $100 \le q \le 200$ kW m^{-2}, $400 \le G \le 700$ kg m^{-2} s^{-1}, $250 \le q/G \le 500$ J kg^{-1}.

[3] The minimal entrance length was calculated using a Reynolds-based correlation for smooth pipes [20] at sub-cooled conditions. The results remained below 50 diameters for Reynolds numbers up to 10^6. The inlet Reynolds numbers in the present data lie at 10^4.

[4] Method followed by several authors [9,27] during experimental work and recommended by Kurganov [19].

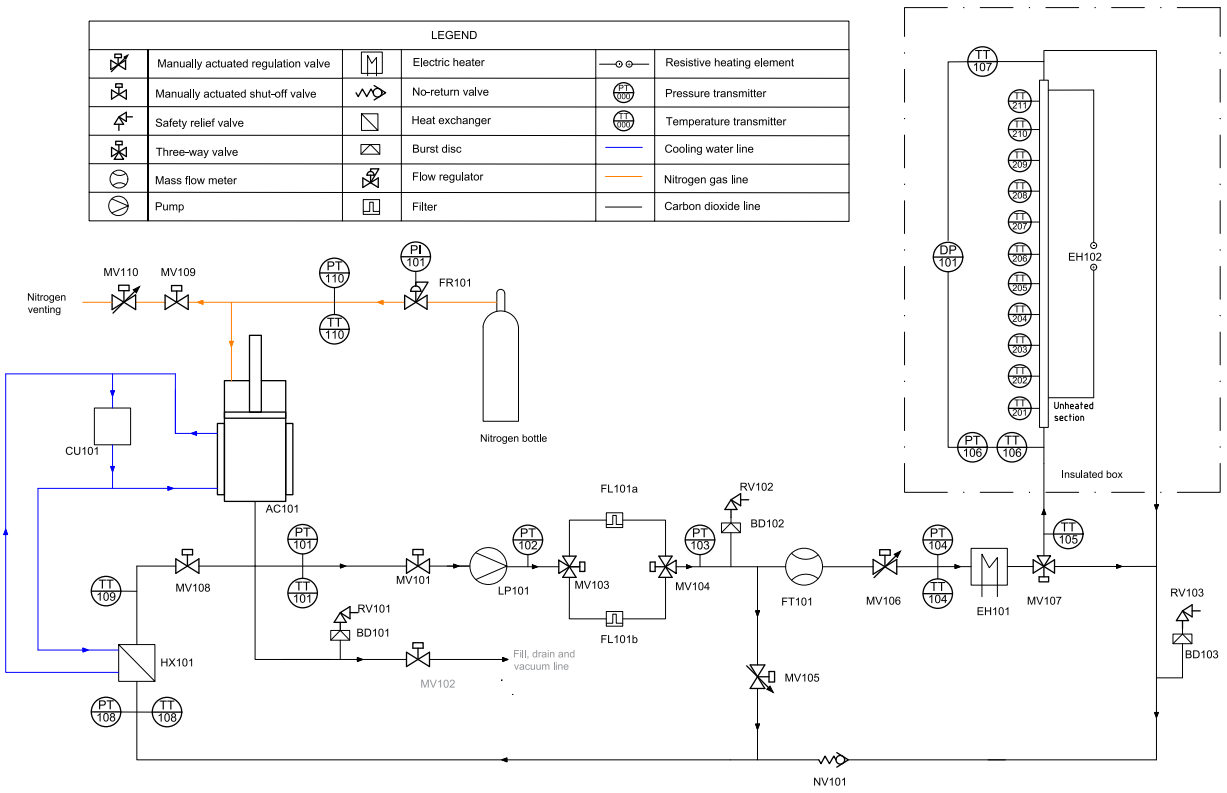

Fig. 3. Process and instrumentation diagram of CO2-SASS.

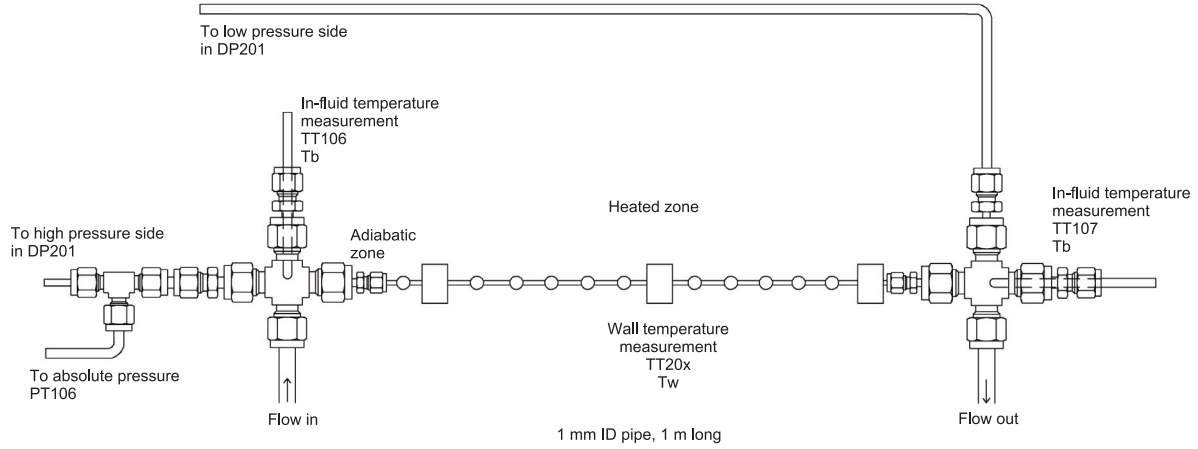

Fig. 4. Test section used for this study.

voltage applied–, and a conservative thermal efficiency of 90% was assumed to consider environmental heat losses at data points where the power absorbed was larger than the power provided to the pipe. Such data points were four setpoints at 7.5 MPa, from an inlet temperature of 24.5 °C. A heat balance was carried out in order to estimate the heat leaks, which resulted 2 W at 29 °C. This accounts for all contributions from the environment and from the effect of axial conduction through the metallic pipes.

Once the heat flow absorbed by the fluid is known, the pipe length can be discretized in N segments with length dz, where $dz = L/N$ so that the enthalpy value along the axial pipe dimension can be calculated as:

$$h_{z+dz} = h_z + \frac{d\dot{Q}}{\dot{m}}, \tag{2}$$

where

$$d\dot{Q} = \frac{\dot{Q}}{L_{\text{heater}}} dz. \tag{3}$$

To ensure the results were independent of the numerical discretization, a grid independence study was carried out for the axial enthalpy integration. The number of segments was varied from $N = 30$ to $N = 500$ and at $N > 60$ the shift in the total calculated pressure drop was less than 0.1%. The difference in the peak value between $N = 60$ and $N = 100$ was 3.5% due to the extreme property gradients at the pseudo-critical point. $N = 100$ was used for higher resolution.

The pressure at each pipe axial position is calculated after each segment. Frictional pressure drop is estimated using the Darcy–Weisbach equation (Eq. (5)), for which the Darcy friction factor (Eq. (7)) can be obtained from the empirical equations [28] after calculating the

Table 2
Dimensions of the test section and measurement accuracies.

Dimensions	Value	Units
Tube length	1	m
Inner diameter	1.037	mm
Outer diameter	1.591	mm
Heated length	903	mm
Start of heater length	70	mm
Average roughness	1.15	μm
Name of test section	TS001A	–
Accuracy	**Value**	**Units**
Absolute pressure (CO_2)	0.02	MPa
Absolute pressure (N_2)	0.03	MPa
Differential pressure	0.3	kPa
Fluid temperature	0.05	K
Wall temperature	0.07	K
Mass flow	0.036	g/s
Diameter	0.0007	mm
Length	Negligible	–
Sensor name	**Type of sensor**	**Location (m)**
TT201	Thermocouple type K	Pipe wall, $z = 0.03$
TT202	Thermocouple type K	Pipe wall, $z = 0.14$
TT203	Thermocouple type K	Pipe wall, $z = 0.22$
TT204	Thermocouple type K	Pipe wall, $z = 0.31$
TT205	Thermocouple type K	Pipe wall, $z = 0.39$
TT206	Thermocouple type K	Pipe wall, $z = 0.48$
TT207	Thermocouple type K	Pipe wall, $z = 0.56$
TT208	Thermocouple type K	Pipe wall, $z = 0.65$
TT209	Thermocouple type K	Pipe wall, $z = 0.73$
TT210	Thermocouple type K	Pipe wall, $z = 0.82$
TT211	Thermocouple type K	Pipe wall, $z = 0.90$
TT106	In-fluid PT-100	Right before entering the test section
TT107	In-fluid PT-100	Right after leaving the test section

Reynolds number (Eq. (4)). For this work, the flow was always turbulent, therefore only turbulent friction factors have been included in the data reduction procedure. For a pipe with 1.5 μm roughness, the Haaland explicit solution of Colebrook–White equation can be used, shown in Eq. (7). Even though the model accounts for axial property evolution via discrete segments, radial property variations are not being accounted for in the friction factor calculation. Wang et al. [29] compared the performance of several radially corrected empirical relations with isothermal ones and concluded that isothermal models could be applied to small pipes. Larger diameter tubes can be more significantly affected by radial distribution of properties and, although this is also influenced by additional parameters–heat flux, mass flux, among others–, the present model yields satisfactory results.

Pressure drop due to flow acceleration is calculated with Eq. (6). The total pressure drop is calculated as the sum of the two.

$$Re_z = \frac{v_i D_z \rho_z}{\mu_z} \tag{4}$$

$$\Delta p_{frict,\Delta z} = \frac{f_z \rho_z v_z^2}{2 D_i} \Delta z \tag{5}$$

$$\Delta p_{acc,\Delta z} = G^2 \left(\frac{1}{\rho_{z+1}} - \frac{1}{\rho_z} \right) \tag{6}$$

Due to the non-linearity of the physical properties, an iterative method was used to ensure convergence of the local property values, with a convergence tolerance of $1 \cdot 10^{-8}$ bar.

$$f = \left[-1.8 \log_{10} \left(\left(\frac{\epsilon}{3.7 D_i} \right)^{1.11} + \frac{6.9}{Re_z} \right) \right]^{-2} \tag{7}$$

The outlet pressure value obtained with the iteration agreed with the outlet pressure derived from $p_{out} = p_{PT106} - \Delta p_{DP101}$, with deviations below 0.3%. Once pressure and bulk fluid enthalpy are known along the pipe length, the temperature can be obtained using REFPROP.

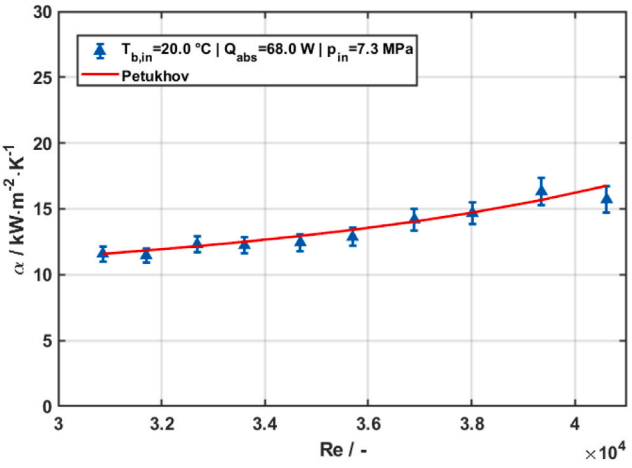

Fig. 5. Comparison of heat transfer coefficient obtained experimentally with the Petukhov correlation in a 1 mm pipe with 1.8 g/s mass flow (corresponding to 2130 kg m^{-2} s^{-1}) and a power of 68 W over a 0.9 m length. Validation tests performed with subcooled carbon dioxide at pressure below the critical point.

To calculate the heat transfer coefficient, the bulk fluid temperature at which the outer wall temperatures are measured are obtained by interpolation. The temperature difference across the wall of a hollow cylinder with outer diameter D_o and inner diameter D_i with heat generation within the pipe volume can be calculated with Eq. (8).

$$T_{w,o} - T_{w,i} = \frac{q D_i}{4 \lambda_{SS}} \left(\frac{\phi(1 - ln\phi) - 1}{1 - \phi} \right), \text{ where } \phi = \left(\frac{D_o}{D_i} \right)^2 \tag{8}$$

The thermal conductivity of stainless steel is considered constant throughout the range of temperatures (20–40 °C). Once the two temperatures are known, the *local* heat transfer coefficient can be calculated using Eq. (9).

$$\alpha = \frac{q}{T_{w,z} - T_{b,z}} \tag{9}$$

4.2. Data repeatability and uncertainty

The reliability of the measurements obtained with the present test rig has been preliminarily validated by comparing measurements performed in the subcooled liquid region with the well accepted correlation by Petukhov [22]. Further details of this validation are reported in [21].

A sensitivity analysis was performed to assess the model dependence of the local heat transfer coefficient on the assumed friction factor correlation and on local pressure uncertainty. Replacing the Haaland [30] correlation with Petukhov [22] or McAdams [31] (smooth pipe) resulted in a maximum deviation of 13.9% and 12.8% in α, respectively. However, using Swamee–Jain [32] instead of Haaland resulted in a maximum deviation of 1.5% in α. In general, Haaland is an accepted model in supercritical literature [29] for small pipes.

Fig. 5 shows the experimental heat transfer coefficient, as well as the one calculated with Petukhov versus the Reynolds number. The trend of the experimental data follows well that of the calculated values, showing very good agreement with a well established theoretical model. The roughness of the pipe was accounted for in the friction factor used.

A second validation of this test rig was performed in the supercritical regime, by replicating a number of data points acquired by Theologou et al. [8] in a 4 mm pipe, using the test facility SCARLETT [33]. The results are shown in Fig. 6. Although the measurements with CO2-SASS were performed in this case with a middle thermocouple, data suggest good agreement in the magnitude of the heat transfer coefficient. Best agreement is observed in the liquid-like region,

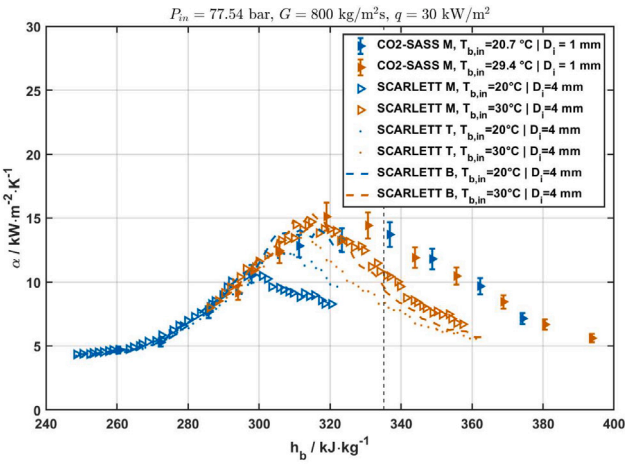

Fig. 6. Heat transfer coefficient data obtained with CO2-SASS at similar conditions as reported by SCARLETT in Theologou et al.'s work [8]; B = bottom, M = middle, T = top. Operating pressure is 7.74 MPa.

as values only start diverting when the bulk enthalpy approaches the pseudo-critical area. On this note, it is interesting to consider that the only difference between SCARLETT and CO2-SASS data is the diameter, suggesting that the differences found might be caused by buoyancy effects in the larger pipe.

The uncertainty of the heat transfer coefficient is calculated using the Taylor series propagation of uncertainty. The resulting derived uncertainty includes mass flow contribution, enthalpy sensitivity, geometry and thermal gradient effect. The total relative error can be calculated using Eq. (10).

$$\frac{u_\alpha}{\alpha} = \left[\left(\frac{u_{\dot m}}{\dot m}\right)^2 + \frac{\sum_{i\in\{in,out\}} \left[\left(c_{p,i} u_{T_i}\right)^2 + \left(\left(\frac{\partial h}{\partial P}\right)_{T_i} u_{P_i} \right)^2 \right]}{(h_{out} - h_{in})^2} + \left(\frac{u_A}{A}\right)^2 + \frac{u_{T_w}^2 + u_{T_b}^2}{(T_w - T_b)^2} \right]^{1/2} \tag{10}$$

For the propagation, the procedure described in detail in [21] is used. The contribution of the impurity concentration to the total uncertainty can be added in the final uncertainty, as it affects the enthalpy calculation at both inlet and outlet conditions. Evaluating the sensitivity $(\partial h/\partial x_{N_2})_{T,P}$ numerically via central differences in REFPROP at the nominal composition of 200 ppm N_2, the contribution of the uncertainty in the purity to the enthalpy uncertainty reads:

$$\left(u_{h,x}\right)^2 = \sum_{i\in\{in,out\}} \left[\left(\frac{\partial h}{\partial x_{N_2}}\right)_{T_i,P_i} u_{x_{N_2}} \right]^2 \tag{11}$$

A conservative approach is taken and the error in x_{N_2} at the inlet and the outlet are considered uncorrelated in Eq. (11). Total uncertainties at different system conditions, resulting in the combination of Eqs. (10) and (11) are shown by means of error bars in Fig. 8. It can be observed that, when far away from the pseudo-critical point (calculated at inlet pressure) the uncertainty is less than 5%, however when approaching that point it increased significantly.

Each set of operating conditions was measured twice. Each measurement is averaged over 300 steady-state points. Fig. 7 shows heat transfer coefficient data acquired in two independent repetitions executed in different days. It can be noted that all differences are well within the uncertainty.

To be noted, although not shown in the current manuscript, the relative error in the pressure drop measurement between two sets of measurements was less than 1% in cases at identical testing conditions.

5. Results

In this work, the Widom line was determined from the c_p maxima at each system pressure using a second-order polynomial fit, and is used throughout the analysis to identify the Widom line for each measurement inlet condition. The fit was performed for the range 7.5–10 MPa and the resulting equation was:

$$T_m(p_{in}) = -248.74 + 9.13 p_{in} - 0.22 p_{in}^2 \tag{12}$$

where p_{in} is in MPa and T_m in degree Celsius.

5.1. Buoyancy effect

Fig. 9 compares the heat transfer coefficients obtained in the 1 mm pipe under similar inlet conditions, obtained from two different locations: the top of the tube (TC0) and the side (TC90). As shown, all differences are well within the measurement uncertainty. The largest discrepancy between the measurements occurs at 7.5 MPa inlet pressure, near the pseudo-critical point (between 320 and 340 kJ/kg bulk enthalpy); and at 8.0 MPa, around 340 kJ/kg.

In supercritical flow, the threshold generally calculated for discerning between a buoyancy affected flow from one free of buoyancy effects is the Richardson number or a modified version of it [34]. For horizontal flows, flow conditions that satisfy $\mathrm{Ri} = \mathrm{Gr}/\mathrm{Re}^2 < 10^{-3}$ are said to be free of buoyancy effects. For the data in this article, the Richardson number was marginally above that threshold (around 0.0032) in data points at 7.5 MPa and between $h_b = 320 - 340$ kJ/kg. The remaining data were always below that threshold, around 10^{-4} at 8.0 MPa and 10^{-5} at 8.5 MPa.

However, as discussed previously, the uncertainty is higher at pressures closer to the critical point and at temperatures near the pseudo-critical region. In contrast, at higher pressures (8.5 MPa), no noticeable difference was observed between the two measurement points. Therefore, this differences observed at lower pressures could also be attributed to measurement uncertainty and does not necessarily imply a significant temperature difference.

5.2. Wall temperature profile

The wall temperature profiles shown in Fig. 10 exhibit a mild curvature as the bulk enthalpy approaches the pseudo-critical value. This behaviour originates from the strong thermophysical-property gradients near the pseudo-critical region, where the rapid rise in heat capacity reduces the rate of wall-temperature increase for a given heat flux. Yamagata et al. [13] demonstrated that such property-driven moderation of the wall temperature leads to a local enhancement in heat transfer when buoyancy is weak. It can also be seen that the slope of the bulk temperature evolution with enthalpy is very positive when far away from the pseudo-critical point and it flattens as this point is approached. This shows the increasing heat capacity at such conditions. The difference between wall and bulk temperature decreases as the temperature increases towards the pseudo-critical value, showcasing an increasing heat transfer coefficient. This difference is smaller at lower pressures.

A clear dependence of the wall-temperature evolution on the inlet temperature is observed in all cases. This agrees with the findings of Kline et al. [12], who showed that the axial shape of the wall-temperature profile is highly sensitive to the inlet temperature even when all other operating parameters are fixed. In the present data, varying T_{in} shifts the point at which the wall crosses the pseudo-critical region.

Unlike the behaviour reported by Kline et al. [12] at lower mass fluxes, no temperature spikes or abrupt changes in slope were observed, even for inlet temperatures closest to the pseudo-critical enthalpy. This difference is attributed to the much higher mass flux used here $G = 2130\ \mathrm{kg\,m^{-2}\,s^{-1}}$, combined with the low heat flux $q = 35\ \mathrm{kW\,m^{-2}}$,

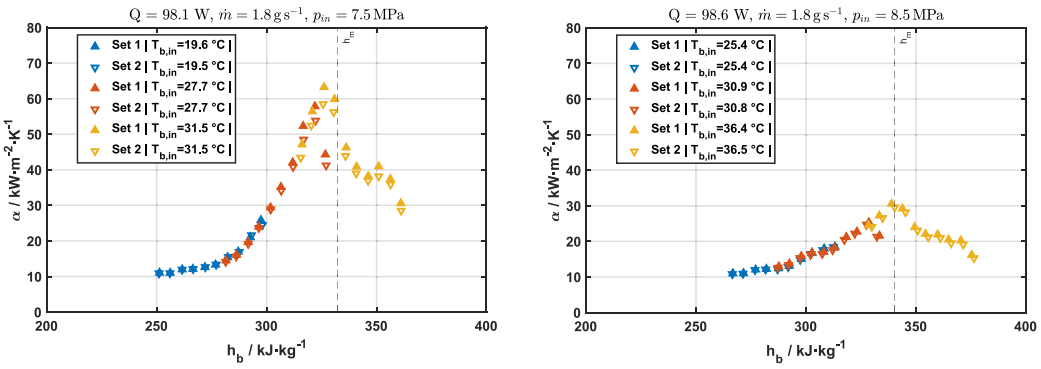

(a) 7.5 MPa (b) 8.5 MPa

Fig. 7. Local heat transfer coefficient along the test section in two experiment independent repetitions (Set 1 and Set 2), reported for two different pressures.

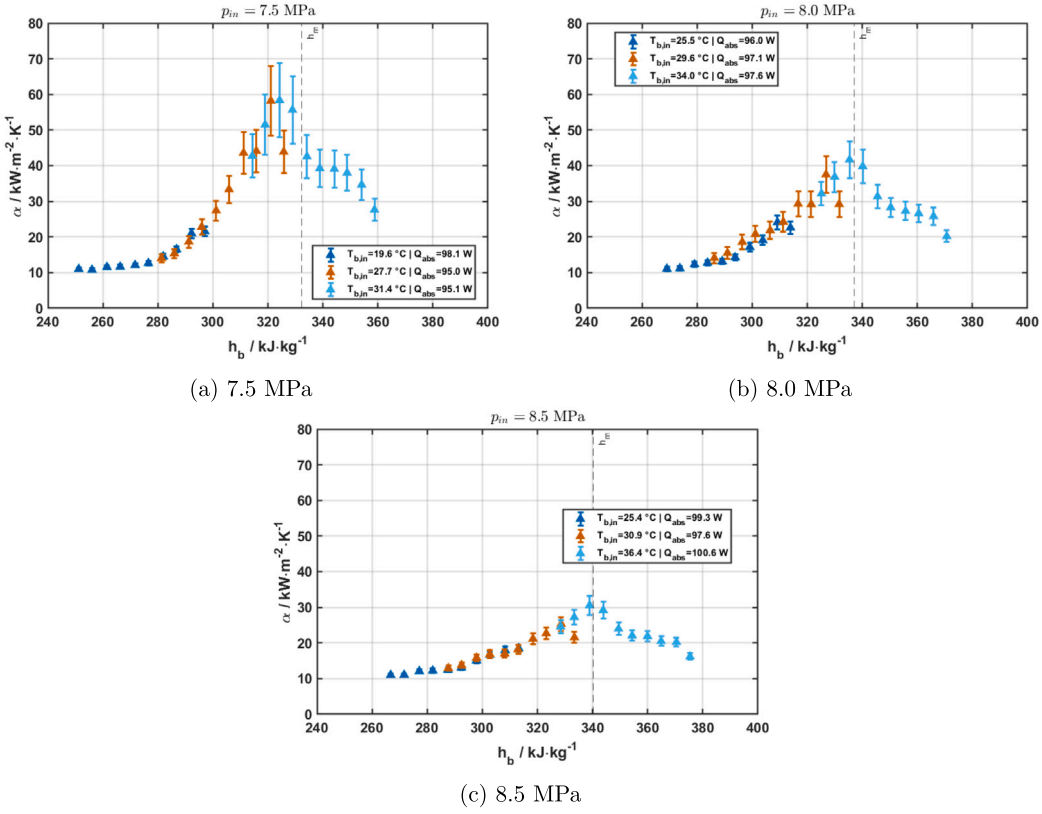

(a) 7.5 MPa (b) 8.0 MPa

(c) 8.5 MPa

Fig. 8. Uncertainty at different inlet pressure and temperature.

resulting in a q/G of only 14 J/kg. Under such conditions, the boundary layer remains well mixed and Heat Transfer Deterioration (HTD) mechanisms are strongly suppressed, consistent with the trends reported by Pioro [35] for high-Reynolds-number water experiments.

5.3. Heat transfer coefficient

From a physical standpoint, the heat transfer coefficient governs the wall-bulk temperature difference for a given heat flux and therefore determines the wall temperature T_w. In the present experiments, however, the heat transfer coefficient is not measured directly, but derived from the measured wall and bulk temperatures through Eq. (9). As a result, variations in the heat transfer coefficient manifest experimentally as variations in the wall–bulk temperature difference, even though the underlying causality remains that the convective transport processes determine α, and hence ΔT.

As discussed in Pedano-Medina et al. [21] and confirmed by the uncertainty analysis shown in Fig. 8, the local heat transfer coefficient becomes highly sensitive when the wall–bulk temperature difference $\Delta T = T_w - T_b$ is small. In this regime, even modest variations in either wall or bulk temperature result in large variations in the calculated heat transfer coefficient. Although this sensitivity amplifies the apparent scatter, clear and systematic trends are observed at all three pressures. Fig. 11 shows the evolution of the local heat transfer coefficient as a function of bulk enthalpy for all operating conditions investigated in this work. It can be seen that when the temperature is on the left of the pseudo-critical, all datapoints converge towards similar values. As the pseudo-critical temperature is approached, the trends diverge.

Indeed, at conditions far from the pseudo-critical point, the heat transfer coefficient remained nearly constant at approximately 10 kW m^{-2} K^{-1} along the pipe for all system pressures. As the bulk enthalpy increased towards 300 kJ kg^{-1}, the heat transfer coefficient

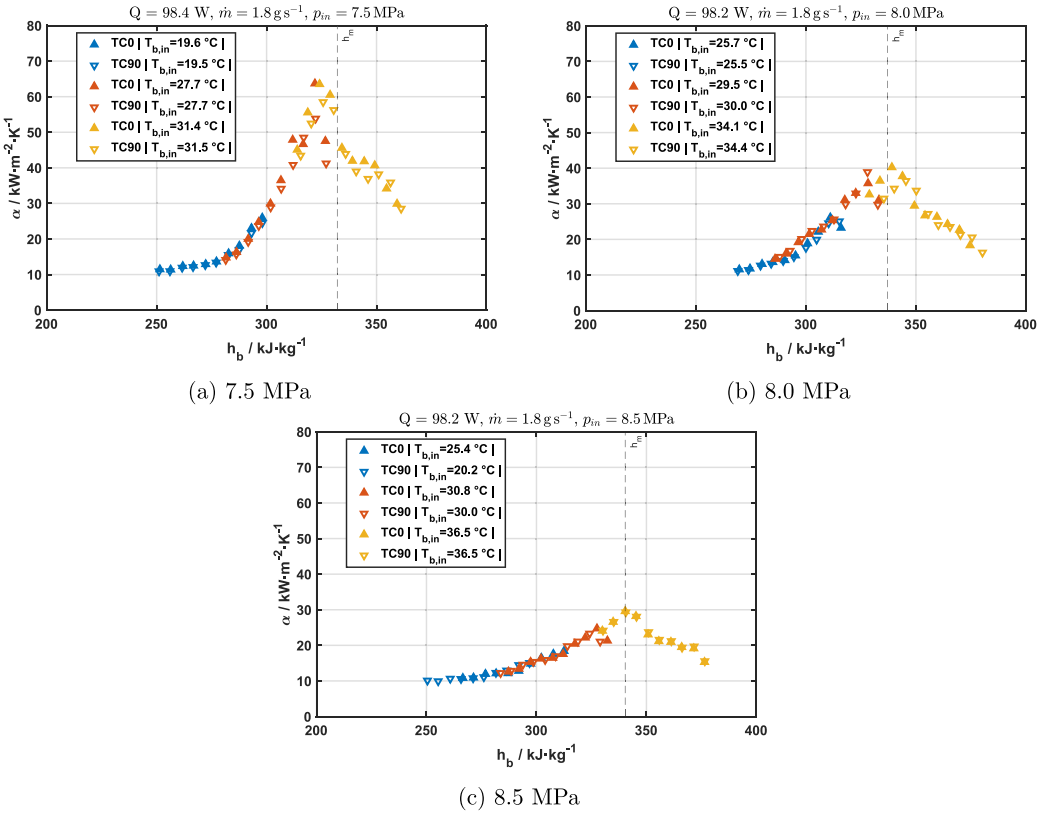

Fig. 9. Comparison between the heat transfer coefficients obtained at the top (TC0) and middle generatrix (TC90) of the pipe at several inlet conditions.

began to rise, reaching a local maximum with larger magnitude at lower pressures. This peak occurred when the wall temperature crossed the pseudo-critical temperature. A similar local maximum was observed at all system pressures as the bulk enthalpy approached the pseudo-critical value.

As the inlet temperature increased further, a new heat transfer coefficient profile appeared, showing two local peaks forming an M-shape. This behaviour is similar to that reported by Wang et al. [9], although their heat transfer coefficients were lower due to the lower mass flow rate (0.6 g s^{-1}) and significantly higher heat fluxes. Very similar trends were shown by Wang et al. [27] in a 4.6 mm inner diameter pipe. In the current work, the overall shape remained similar for all cases with inlet temperature above 30 °C, although the slope changed in some cases. When the inlet temperature was slightly below the pseudo-critical and the pressure was 8.5 MPa, the heat transfer coefficient remained nearly constant, mirroring the trend of the specific heat capacity at that pressure.

When the flow entered the test section at the pseudo-critical temperature, the evolution of the heat transfer coefficient with enthalpy was negative. Heat transfer coefficient data resemble the evolution of the specific heat capacity, increasing before the pseudo-critical temperature and decreasing afterwards. However, the M-shaped profile appeared when both the wall and the bulk crossed the pseudo-critical values. This local increase in the heat transfer coefficient could be due to flow acceleration caused by bulk density decrease. The acceleration parameter Ac_b was calculated as per Jackson's definition [14] as shown in Eq. (13):

$$Ac_b = \frac{E_b}{Re_b^{1.625} Pr_b}, \tag{13}$$

where

$$E_b = \frac{q\,\beta_b\,D}{\lambda_b}. \tag{14}$$

The value Ac_b ranged between 0.5×10^{-4} and 2×10^{-4}, above the 4×10^{-6} threshold proposed by Jackson and Hall [25], indicating that bulk flow acceleration affects the Nusselt number in the data presented. However, the classical acceleration parameter $K = \frac{\nu}{u^2}\frac{du}{dx} \sim 10^{-8}$ [36] was below the relaminarization threshold of 3×10^{-6}, suggesting that although acceleration modifies the heat transfer, it is not sufficient to relaminarize the flow. The M-shaped profile could be caused by the combined effect of density and heat capacity.

Finally, the effect of pressure is clear across all data points: as pressure increases from 7.5 to 8.5 MPa, the highest convective heat transfer coefficient attainable decreases and shifts towards higher bulk enthalpy values. Despite the variations in magnitude, all pressures exhibit a similar qualitative trend. Other authors observed no effect from operating pressure at higher q/G [10], however in this present case the heating is moderate for the high mass flux, thus allows the influence of pressure to be observed.

5.4. Correlations

Six correlations are evaluated in this study: Petukhov's theoretically derived correlation (P) [31], the empirical Krasnoshchekov–Kuraeva–Protopopov[5] (from now on, the KKP) correlation [24], the empirical correlations by Wang et al. [9] (W) and Guo et al. [10] (G), developed for small pipes in horizontal flow, and two correlations by Jackson [26]. Their expressions and applicability ranges are summarized in Table 1. Reynolds numbers for the experimental tests ranged from 10^4 to 10^5.

Fig. 13 shows the comparison between experimental and predicted heat transfer coefficients, where the dashed lines represent ±20%

[5] In the literature, this correlation is usually referred to as Krasnoschekov–Protopopov, however the article from 1969 has I.V. Kuraeva as the second author.

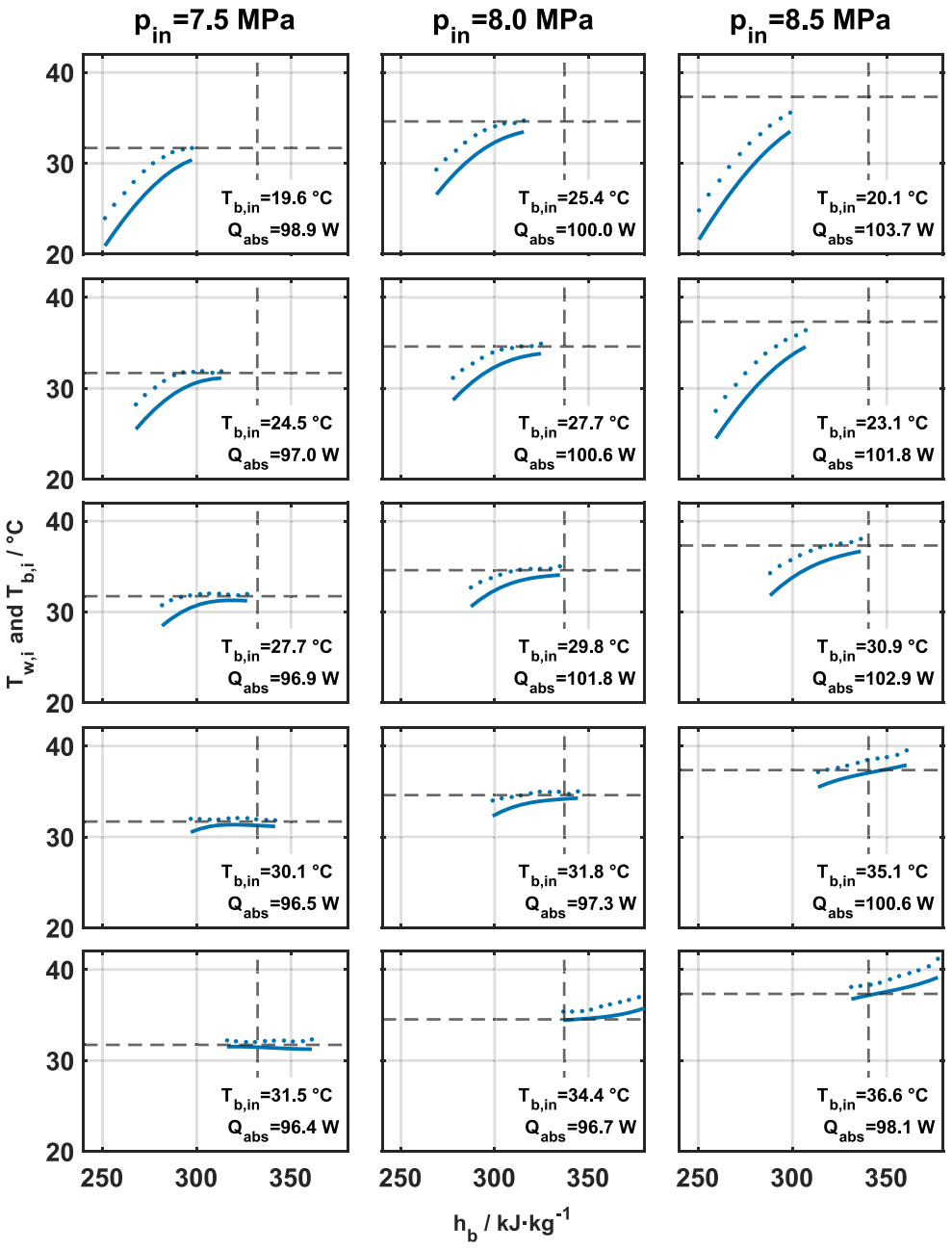

Fig. 10. Local wall ($T_{w,i}(h_b)$, dotted line) and bulk ($T_{b,i}(h_b)$, solid line) temperature profiles versus the bulk enthalpy (h_b) for all operating conditions. Q_{abs} is the calculated $\dot{Q}$. Left = 7.5 MPa, centre = 8.0 MPa, right = 8.5 MPa. The dashed lines represent the pseudo-critical values of each variable, calculated at the inlet pressure.

ranges. In general, the KKP correlation performs best at the present conditions, with approximately 85% of the data falling within ±20%. The Petukhov correlation tends to systematically overpredict the heat transfer coefficient. In the latter, 63% of the data fell within ±20%. This discrepancy arises because the Petukhov formulation assumes radially homogeneous properties evaluated at the bulk temperature and therefore cannot account for the steep radial variations occurring near the pseudo-critical region. The evaluation of the properties assuming a uniform bulk profile does not consider the physics behind supercritical flows and therefore ignores the different physical state that the wall and bulk are in. Due to the sharp proportionality of the Nusselt number to the Prandtl number in this correlation, the Prandtl number increases sharply when the pseudocritical temperature is approached and drives the predicted result, thus overestimating performance by ignoring the insulating effect of the low-density wall layer.

The KKP correlation, in turn, introduces a correction to the Petukhov formulation via the property ratios $(\overline{c}_p/c_{p,b})^n$ and ρ_w/ρ_b, intended to account for those radial variations. $\overline{c}_p$ is the radially-averaged heat capacity, calculated as shown in Table 1. These allow the correlation to capture part of the enhancement near the pseudo-critical point. At 7.5 MPa, where the pseudo-critical c_p peak is especially sharp, the correlation reproduces a mild increase that qualitatively resembles the first peak observed in the experimental heat transfer coefficient. However, it fails to fully reproduce the local peak in heat transfer coefficient. Fig. 14 shows three representative cases at 35 kW m^{-2} and G = 2130 kg m^{-2} s^{-1}. At 7.5 MPa, Petukhov overpredicts the experimental data and KKP captures well the qualitative trend near the pseudo-critical enthalpy, however does underpredict the local peak in heat transfer coefficient. At 8 MPa and 8.5 MPa, similar behaviours are observed, however the Petukhov correlation seems to reach a better

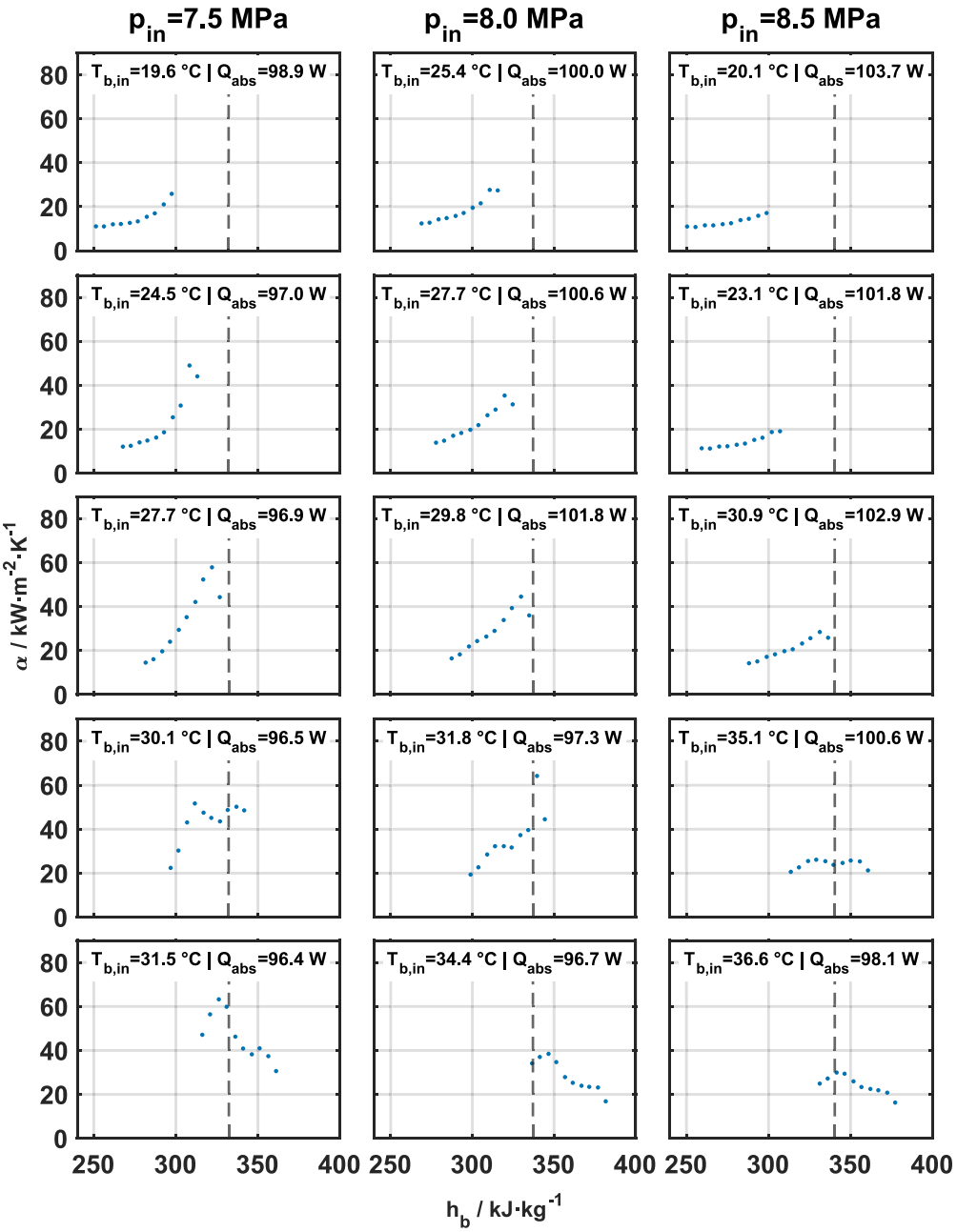

Fig. 11. Heat transfer coefficient profiles, $\alpha(h_b)$, for all operating conditions. Q_{abs} is the calculated $\dot{Q}$. Left = 7.5 MPa, centre = 8.0 MPa, right = 8.5 MPa.

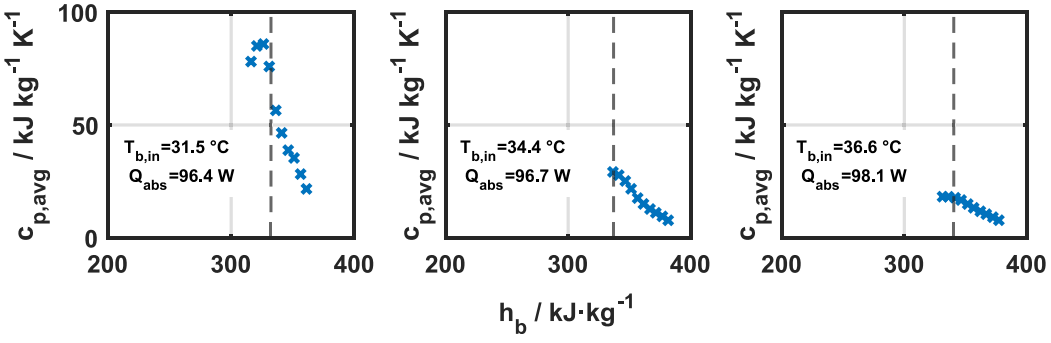

Fig. 12. Correction term $\bar{c}_p$ at the vicinity of the pseudo-critical point. Left = 7.5 MPa, centre = 8.0 MPa, right = 8.5 MPa.

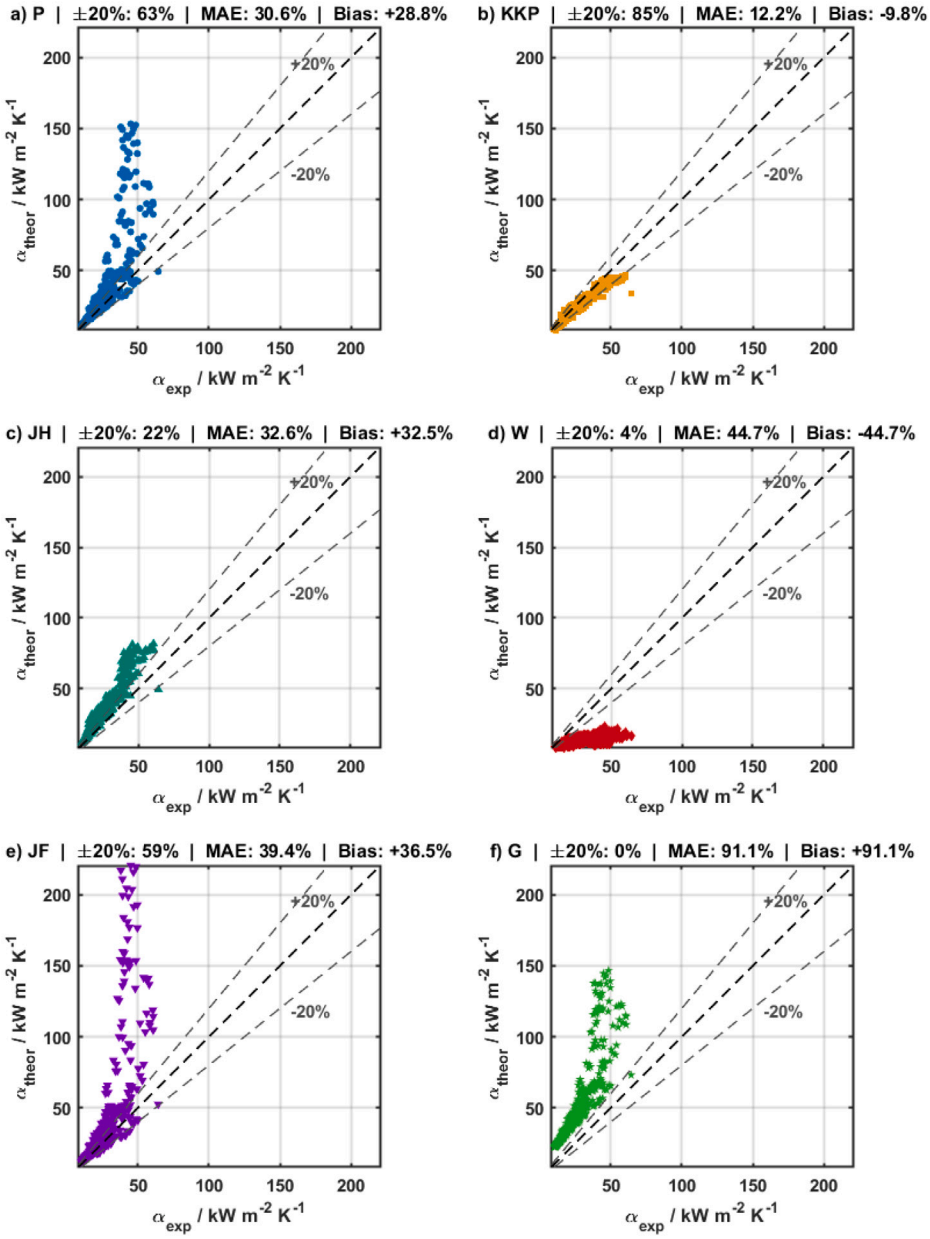

Fig. 13. Comparison between experimental and predicted heat transfer coefficients (α) for all tested correlations. The dashed lines indicate a ±20% error band. Performance metrics for each model are provided in the individual titles, including the percentage of data within the ±20% range, Mean Absolute Error (MAE), and Bias. (a) Petukhov (P), (b) Krasnoshchekov–Kuraeva–Protopopov (KKP), (c) Jackson and Hall (JH), (d) Wang et al. (W), (e) Jackson and Fewster (JF), and (f) Guo et al. (G).

result than at 7.5 MPa. This highlights the sensitivity of the correlation to the peak in Prandtl number, which is much sharper at 7.5 MPa.

Fig. 12 illustrates the variation of the radially averaged heat capacity. It can be seen that at 7.5 MPa, the $\bar{c}_p$ peaks sharply near the pseudo-critical enthalpy, driving the predicted local peak. At 80 and 8.5 MPa, the peak becomes progressively weaker and broader (and decreases more linearly with enthalpy), reducing the correction magnitude. The exponent n of the correlation is rather constant with pressure and totals around 0.4 for the present dataset. At higher T_w/T_m, the coefficient increases. In addition, the density ratio sees a local minimum in the vicinity of the pseudocritical temperature at 7.5 MPa, and further allows the model to predict the behaviour.

The W correlation only predicted 3% of the data within 20%. Although most conditions satisfy the applicability requirements, heat fluxes in this study are lower. Even if the heat flux influence may be partially captured through the averaged specific heat ratio, the correlation under predicts nearly all the experimental data. This is explained by the significantly lower heat flux in this case.

The Guo correlation failed to predict any data point and systematically overpredicted the heat transfer coefficient across all cases. This behaviour could be partially attributed to the Richardson number correction term $(Gr/Re^2)^{-0.125}$: with Richardson numbers between 10^{-5}–10^{-3} in the present dataset, the negative exponent increases the magnitude of the correction in Nu. This makes sense, as the G correlation was developed for lower mass velocities than in the present

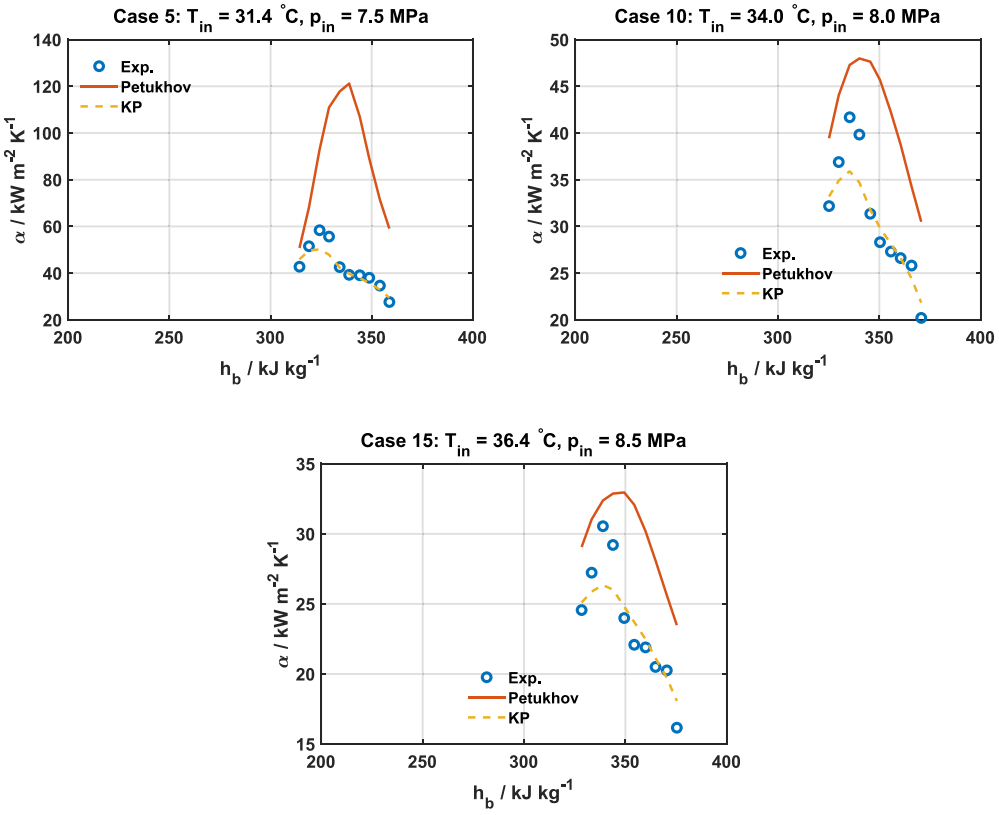

Fig. 14. Comparison of experimental local heat transfer coefficients with Petukhov and KKP correlations for conditions with inlet temperatures close to the pseudo-critical value. Case-specific conditions are specified on top of each figure.

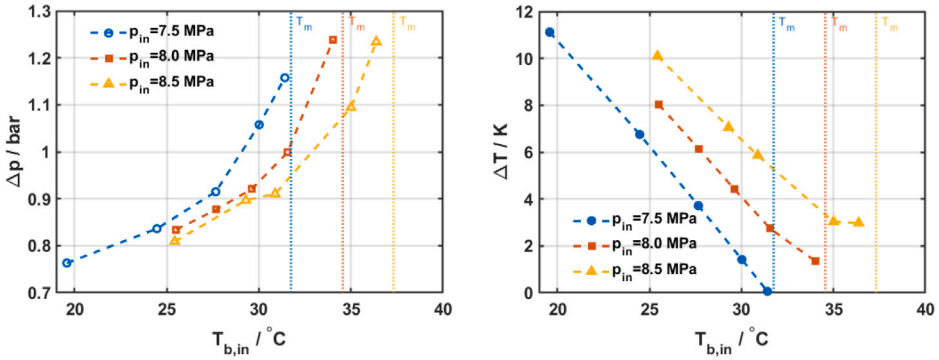

(a) Pressure drop (b) Temperature increase

Fig. 15. Pressure drop and temperature increase at different inlet temperature and pressure. Note: Error bars for Δp and ΔT are omitted as the calculated absolute uncertainties (±0.003 bar and ±0.07 K, respectively) are smaller than the symbol size.

study. In addition, the Prandtl number enhancement is observed in the parity plot, as the result also seems unstable at conditions of high experimental heat transfer coefficient.

Further, the Jackson and Hall (JH) correlation [25] predicted 22% of the data within 20%. Since the data presented lay outside of the applicability requirements, this is not a surprising result. To begin with, Jackson correlation is developed for larger Reynolds numbers. The data for higher enthalpy are the only ones satisfying the condition at Reynolds of about 80 000. The most restrictive applicability condition, however, is the density ratio. A ρ_w/ρ_b between 0.9 and 1 implies very mild property variation along the diameter, achievable with extremely low q/G. In this study, ρ_w/ρ_b sat below 0.9 at most cases. The correlation systematically overpredicts the majority of the data, probably because of the term $Pr^{0.5}$ being large near the pseudo-critical point and also at the vicinity of the pseudo-critical point.

Finally, the simplified correlation of Jackson and Fewster [26] (JF) predicted more data (59%) than the longer version (JH, 22%). In principle, this correlation is a variation of the Dittus–Boelter correlation with a radial density correction, which means that at points where density ratios are not very low and Pr is moderate (at conditions that resemble more a Normal Heat Transfer regime), the correlation behaves just like Dittus–Boelter and predicts well. When Pr becomes large, it dominates the value of Nusselt and shoots the final result up. What is interesting is to see that $\bar{c}_p$, which physically accounts for the asymmetry of enthalpy transport across the cross-section, actually worsens the overall prediction for this dataset. Close to the pseudo-critical point, the ratio is large due to small temperature differences

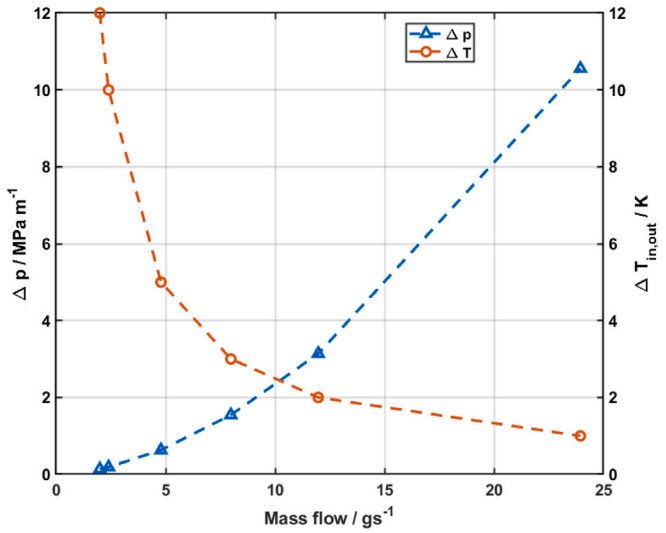

Fig. 16. Calculated pressure drop and temperature increase using water in a 1 mm diameter channel with a dissipated power of 100 W with T_{in} = 30 °C.

for a given enthalpy difference; while at high enthalpy values the ratio falls to below 1 and reduces the predicted value. Finally, can be seen that the correlation seems unstable at high values of experimental heat transfer coefficient due to visible scatter, while the JH correlation remains contained, although over predicting.

The success rates within ±20% and their associated 95% binomial confidence intervals, computed over 60 independent cases (15 cases x 4 experimental runs), are as follows: KKP achieved 85% (95% CI: 73%–93%), Petukhov 63% (95% CI: 50%–75%), JF 59% (95% CI: 45%–71%), JH 22% (95% CI: 12%–34%), W 3% (95% CI: 0%–11%) and G 0%.

5.5. Pressure drop and temperature increase

A final consideration in this dataset in order to characterize the physical mechanisms and the cooling performance at the conditions tested has been the overall pressure drop (Δp) and temperature increase between inlet and outlet of the test section ($\Delta T_{\text{in,out}}$). The results at the testing conditions corresponding to this study are shown in Fig. 15.

The figure shows that the pressure drop increases exponentially when approaching the pseudocritical temperature. As seen in Eq. (5), the frictional pressure drop along a pipe is proportional to the square of the fluid velocity. As can be seen in Fig. 1 and was discussed in Section 1, density drops sharply at the vicinity of the pseudo-critical point and the fluid resembles a gas more than a liquid. This means that for a constant mass flux, the corresponding fluid velocity will be much larger for a smaller density, and therefore the Δp will respond accordingly. On the other hand, the behaviour of the $\Delta T_{\text{in,out}}$ is different, as it is consequence of the heat capacity. It decreases linearly with inlet temperature at a given pressure and reaches a plateau (as can be seen for the data at 8.5 MPa) when approaching the pseudo-critical temperature. In view of the heat capacity trend when surpassing the pseudo-critical point, one would expect that the trend of $\Delta T_{in,out}$ is inverted if the fluid kept being heated, thus forming a U shape.

In summary, the opposing trends observed in Δp and $\Delta T_{\text{in,out}}$ highlight the inherent trade-off between hydraulics and thermal performance when designing a cooling system. While the higher heat capacity in this regime leads to enhanced thermal effectiveness – lower temperature increase along the pipe – it simultaneously results in an increase of pressure drop. However, the relative importance of each aspect will depend on the application itself. For instance, in certain systems, pressure drop might be a limitation – as it is for low-pressure systems – whereas for others the minimization of the temperature increase could be the main aspect to consider. The following section shows how this trade-off becomes particularly relevant when alternative coolants, such as water, are considered.

Finally, in the present data, the acceleration contribution to the total pressure drop accounted for a maximum of 4% and increased as the pseudo-critical temperature was approached at every operating pressure.

5.6. Comparison with water

The only natural coolant that we consider in comparison with carbon dioxide in electronics cooling is water. Others, like ammonia and hydrocarbons, are toxic and/or flammable and therefore present undesirable safety concerns in with systems where electrical current is present. A major advantage of carbon dioxide with respect to water is its non conductive nature. However, the use of water as a default thermal management fluid in Direct Liquid Cooling applications for data centres [37] and other electronics [38] is a reality despite its disadvantages when dealing with small pipes and moderate heat fluxes. To illustrate this, a comparison analysis is performed comparing the flow of water that would be needed to achieve similar conditions as those obtained with carbon dioxide under the present conditions. The $\Delta T_{\text{in,out}}$ was fixed to similar values obtained experimentally with sCO_2 in the present work and the necessary mass flow to absorb 100 W was calculated using Eq. (15), assuming a constant heat capacity of 4.18 kJ kg^{-1} K^{-1} for water.

$$\dot{Q} = mc_p \Delta T_{\text{in,out}} \tag{15}$$

The corresponding pressure drop (in bar m^{-1}) was calculated using Eq. (5). The results are shown in Fig. 16. It can be seen that a flow of 2 g s^{-1} would be the minimum required of water, which would imply a $\Delta T_{\text{in,out}}$ of 12 K. This is quite higher than most of the values achieved with sCO_2.

At these conditions, Re would sit around 3500, corresponding to a transitional flow. Even considering water flow as fully developed turbulent, the heat transfer coefficient would be 10 kW m^{-2} K^{-1}. This is below the minimum values attained with sCO_2, about 30 kW m^{-2} K^{-1} at the present testing conditions.

In order to further decrease $\Delta T_{\text{in,out}}$, the mass flow would have to be increased. Consequently, the pressure drop would increase exponentially with the mass flow. Analyses of this type showcase the difficulties of using water in small diameter channels for cooling. Carbon dioxide could offer a valuable alternative in conditions that demand the use of small pipes, although parameters like the cycle efficiency and overall performance are still to be studied in depth.

6. Conclusions

The present data lie in conditions with low heat flux and high Reynolds numbers, where buoyancy and HTD effects are expected to be weaker than in most published studies. Large increases in wall temperature were not observed in the conditions tested: 1 mm pipe, heat flux of 35 kW m^{-2} and mass flux of 2130 kg m^{-2} s^{-1} and pressures ranging from 7.5 to 8.5 MPa. This regime is of practical interest for electronics cooling, yet poorly documented in the literature.

The heat transfer coefficients obtained covered a wide range–10 kW m^{-2} K^{-1} up to 60 kW m^{-2} K^{-1}–and a clear effect of the physical properties at the pseudo-critical point was observed in the dataset. A first peak in the heat transfer coefficient was observed as the wall fluid approached the pseudo-critical temperature, while a second one was identified in cases where the bulk fluid also surpassed the pseudo-critical enthalpy within the heated area. Wall and bulk temperature profiles were provided, showing that no sudden peaks were observed, demonstrating lack of HTD. The temperature increase along the pipe

and pressure drops were also reported in this study, and their evaluation for the use of sCO_2 was discussed. A calculation of the local pressure profile along the pipe using the Haaland correlation for the friction factor yielded a maximum of 6% error in the pressure drop calculation, when compared to the measured value. Finally, a number of correlations were applied and their applicability was evaluated, showing that the Krasnoschekov–Kuraeva–Propotopov correlation predicted 85% of the data within 20% error. Other correlations that did not account on the radial property distribution significantly overpredicted the heat transfer coefficient.

The data presented here are of great value for the future of electronics cooling using sCO_2 and offer a benchmark for the applicability of turbulent correlations to sCO_2 systems. Additional data in an expanded range of parameters are paramount in order to develop a more generalized model.

While two-phase CO_2 cooling might be the most promising solution for future high-power microelectronics requiring high temperature stability, the present results demonstrate that supercritical CO_2 can offer an attractive and robust alternative for operation at warmer temperature levels. This study expands the range of operating conditions for next-generation electronics cooling where thermal performance, system simplicity and operational stability must be simultaneously addressed. Further, rather than representing competing approaches, two-phase and sCO_2 cooling should be regarded as complementary regimes of a single working fluid. They offer the possibility of covering an exceptionally wide range of operating temperatures, from the triple point of CO_2 up to approximately 45 °C. This work contributes to bridging this gap and presents CO_2 as a versatile cooling solution for future microelectronics and detector systems.

Finally, under the conditions evaluated in this work, carbon dioxide showed clear advantages over water as a coolant for electronics cooling applications in regards to its local performance. Further evaluation of system considerations and cycle assessment remain a pending task in the field in order to provide comprehensive analyses on their respective performance.

CRediT authorship contribution statement

Camila Pedano-Medina: Writing – review & editing, Writing – original draft, Visualization, Validation, Software, Methodology, Investigation, Formal analysis, Data curation, Conceptualization. **Paolo Petagna:** Writing – review & editing, Supervision, Project administration, Funding acquisition, Formal analysis, Conceptualization. **Susanne Gleissle:** Writing – review & editing, Supervision, Conceptualization.

Nomenclature

A	Area (m^2)
Ac	Acceleration parameter (–)
c_p	Isobaric specific heat capacity ($J\,kg^{-1}\,K^{-1}$)
D	Tube diameter (m)
E	Thermal expansion parameter (–)
f	Darcy friction factor (–)
g	Gravitational acceleration ($m\,s^{-2}$)
G	Mass flux ($kg\,m^{-2}\,s^{-1}$)
Gr	Grashof number (–)
h	Specific enthalpy ($J\,kg^{-1}$)
L	Tube length (m)
$\dot{m}$	Mass flow rate ($kg\,s^{-1}$ or $g\,s^{-1}$)
Nu	Nusselt number (–)
p	Pressure (bar)
Pr	Prandtl number (–)
q	Heat flux ($kW\,m^{-2}$ or $W\,m^{-2}$)
$\dot{Q}$	Heat flow rate (W)
Re	Reynolds number (–)
Ri	Richardson number (–)
T	Temperature (°C)
v	Mean velocity ($m\,s^{-1}$)
z	Axial coordinate (m)

Greek symbols

α	Heat transfer coefficient ($kW\,m^{-2}\,K^{-1}$ or $W\,m^{-2}\,K^{-1}$)
β	Thermal expansion coefficient (K^{-1})
Δp	Pressure drop (bar)
ΔT	Temperature difference (K or °C)
λ	Thermal conductivity ($W\,m^{-1}\,K^{-1}$)
μ	Dynamic viscosity (Pa s)
ρ	Density ($kg\,m^{-3}$)
ξ	Petukhov friction factor term (–)
ϕ	Diameter ratio (–)

Subscripts

abs	Absorbed
avg	Averaged
b	Bulk
cr	Critical
exp	Experimental
f	Fluid
i	Inner
in	Inlet
out	Outlet
o	Outer
m	Pseudo-critical
R	Reduced
w	Wall
z	Axial position

Abbreviations

CI	Confidence Interval
DLC	Direct Liquid Cooling
KKP	Normal Heat Transfer
HEP	High Energy Physics

Funding

This project has received funding from the European Union's Horizon 2020 Research and Innovation Programme under Grant Agreement No. 101004761. This work was also supported by the Wolfgang Gentner Programme of the German Federal Ministry of Education and Research (BMBF).

Declaration of competing interest

The authors declare that they have no known competing financial interests or personal relationships that could have appeared to influence the work reported in this paper.

Acknowledgements

The authors would like to thank Jarl Pettersen and Andrzej Baran for their electrical work.

References

[1] I.L. Pioro, Supercritical-fluids thermophysical properties and heat transfer in power-engineering applications, in: I. Pioro (Ed.), Advanced Supercritical Fluids Technologies, IntechOpen, 2020, http://dx.doi.org/10.5772/intechopen.91474.

[2] R.C. Hendricks, R.J. Simoneau, R.V. Smith, Survey of heat transfer to near-critical fluids, in: K.D. Timmerhaus (Ed.), Advances in Cryogenic Engineering, Springer US, Boston, MA, 1995, pp. 197–237, http://dx.doi.org/10.1007/978-1-4757-0513-3_27.

[3] I. Pioro, Introduction and historical development of supercritical water-cooled reactors (SCWRs), 2011.
[4] B.M. Fronk, A.S. Rattner, High-flux thermal management with supercritical fluids, J. Heat Transf. 138 (12) (2016) 124501, http://dx.doi.org/10.1115/1.4034053.
[5] Paolo. Petagna, Bart. Verlaat, Andrea. Francescon, Two-Phase Thermal Management of Silicon Detectors for High Energy Physics | Encyclopedia of Two-Phase Heat Transfer and Flow III, http://dx.doi.org/10.1142/9789813229471_0005.
[6] M. Huber, A. Harvey, E. Lemmon, G. Hardin, I. Bell, M. McLinden, NIST reference fluid thermodynamic and transport properties database (REFPROP) Version 9.1 - SRD 23, 2018, http://dx.doi.org/10.18434/T4/1502528.
[7] EU-Rules - fluorinated greenhouse gases – climate action, https://climate.ec.europa.eu/eu-action/fluorinated-greenhouse-gases/f-gas-legislation_en.
[8] K. Theologou, R. Mertz, E. Laurien, J. Starflinger, Experimental investigations on heat transfer of CO2 under supercritical pressure in heated horizontal pipes, Energy 254 (2022) 124171, http://dx.doi.org/10.1016/j.energy.2022.124171.
[9] L. Wang, Y.C. Pan, J. Der Lee, Y. Wang, B.-R. Fu, C. Pan, Experimental investigation in the local heat transfer of supercritical carbon dioxide in the uniformly heated horizontal miniature tubes, Int. J. Heat Mass Transfer 159 (2020) 120136, http://dx.doi.org/10.1016/j.ijheatmasstransfer.2020.120136.
[10] P. Guo, S. Liu, J. Yan, J. Wang, Q. Zhang, Experimental study on heat transfer of supercritical CO2 flowing in a mini tube under heating conditions, Int. J. Heat Mass Transfer 153 (2020) 119623, http://dx.doi.org/10.1016/j.ijheatmasstransfer.2020.119623.
[11] S. Liao, T. Zhao, An experimental investigation of convection heat transfer to supercritical carbon dioxide in miniature tubes, Int. J. Heat Mass Transfer 45 (25) (2002) 5025–5034, http://dx.doi.org/10.1016/S0017-9310(02)00206-5.
[12] N. Kline, F. Feuerstein, S. Tavoularis, Onset of heat transfer deterioration in vertical pipe flows of CO 2 at supercritical pressures, Int. J. Heat Mass Transfer 118 (2018) 1056–1068, http://dx.doi.org/10.1016/j.ijheatmasstransfer.2017.11.039.
[13] K. Yamagata, K. Nishikawa, S. Hasegawa, T. Fujii, S. Yoshida, Forced convective heat transfer to supercritical water flowing in tubes, Int. J. Heat Mass Transfer 15 (12) (1972) 2575–2593, http://dx.doi.org/10.1016/0017-9310(72)90148-2.
[14] J. Jackson, Fluid flow and convective heat transfer to fluids at supercritical pressure, Nucl. Eng. Des. 264 (2013) 24–40, http://dx.doi.org/10.1016/j.nucengdes.2012.09.040.
[15] H.-f. Cai, Y.-y. Jiang, T. Wang, S.-q. Liang, Y.-m. Zhu, Experimental investigation on convective heat transfer and pressure drop of supercritical CO2 and water in microtube heat exchangers, Int. J. Heat Mass Transfer 163 (2020) 120443, http://dx.doi.org/10.1016/j.ijheatmasstransfer.2020.120443.
[16] H. Huang, Y. Zhai, Z. Li, Y. Li, H. Wang, Thermal management for microelectronic chips under non-uniform heat flux with supercritical CO2, Int. J. Heat Mass Transfer 236 (2025) 126271, http://dx.doi.org/10.1016/j.ijheatmasstransfer.2024.126271.
[17] Q. Ren, Q. Qiu, Y. Liu, Y. Peng, P. Li, X. Zhu, Experimental investigation of supercritical CO2 heat transfer characteristics in a three-rod bundle, Int. J. Heat Mass Transfer 247 (2025) 127141, http://dx.doi.org/10.1016/j.ijheatmasstransfer.2025.127141.
[18] R.-N. Xu, F. Luo, P.-X. Jiang, Buoyancy effects on turbulent heat transfer of supercritical CO2 in a vertical mini-tube based on continuous wall temperature measurements, Int. J. Heat Mass Transfer 110 (2017) 576–586, http://dx.doi.org/10.1016/j.ijheatmasstransfer.2017.03.063.
[19] V. Kurganov, Yu.A. Zeigarnik, I. Maslakova, Heat transfer and hydraulic resistance of supercritical-pressure coolants. Part II: Experimental data on hydraulic resistance and averaged turbulent flow structure of supercritical pressure fluids during heating in round tubes under normal and deteriorated heat transfer conditions, Int. J. Heat Mass Transfer 58 (1–2) (2013) 152–167, http://dx.doi.org/10.1016/j.ijheatmasstransfer.2012.10.072.
[20] F.M. White, Fluid Mechanics, seventh ed., in: McGraw-Hill Series in Mechanical Engineering, McGraw-Hill, New York, 2011.
[21] C. Pedano-Medina, P. Petagna, S. Gleissle, CO2-SASS: A modular test rig for the scientific assessment of heat transfer of carbon dioxide in the supercritical state, 2025, http://dx.doi.org/10.3390/hardware4020007.
[22] B.S. Petukhov, V.A. Kurganov, A.I. Gladuntsov, Heat transfer in turbulent pipe flow of gases with variable properties, 5 (4) (1973).
[23] V. Gnielinski, New Equations for Heat and Mass Transfer in the Turbulent Flow in Pipes and Channels, NASA STI/Recon Technical Report A, Vol. 41, 1975, pp. 8–16.
[24] E.A. Krasnoshchekov, I.V. Kuraeva, V.S. Protopopov, Experimental studying of carbon dioxide heat transfer in supercritical region under high temperature differences 4 (3) (1966).
[25] J.D. Jackson, W.B. Hall, Forced convection heat transfer to fluids at supercritical pressure, in: Turbulent Forced Convection in Channels and Bundles: Theory and Applications To Heat Exchangers and Nuclear Reactors, Vol. 2, Hemisphere Publishing Corporation, New York, pp. 563–612.
[26] D. Jackson, W.B. Hall, J. Fewster, A. Watson, M.J. Watts, Heat Transfer to Supercritical Pressure Fluids. Part II: Critical Reviews with Design Recommendations, Tech. Rep., Simon Engineering Laboratories, University of Manchester, Didcot, Oxon, OX11 ORA, 1975.
[27] X. Wang, L. Yang, B. Xu, Z. Chen, Experimental study on heat transfer and flow characteristics of supercritical CO2: In-depth analysis of three heat transfer coefficients, Int. J. Heat Mass Transfer 241 (2025) 126748, http://dx.doi.org/10.1016/j.ijheatmasstransfer.2025.126748.
[28] Z. Wang, B. Sun, J. Wang, L. Hou, Experimental study on the friction coefficient of supercritical carbon dioxide in pipes, Int. J. Greenh. Gas Control. 25 (2014) 151–161, http://dx.doi.org/10.1016/j.ijggc.2014.04.014.
[29] L. Wang, Y.C. Pan, J.D. Lee, Y. Wang, B.R. Fu, C. Pan, Experimental investigation in the pressure drop characteristics of supercritical carbon dioxide in the uniformly heated horizontal miniature tubes, J. Supercrit. Fluids 162 (2020) 104839, http://dx.doi.org/10.1016/j.supflu.2020.104839.
[30] S.E. Haaland, Simple and explicit formulas for the friction factor in turbulent pipe flow, J. Fluids Eng. 105 (1) (1983) 89–90, http://dx.doi.org/10.1115/1.3240948.
[31] B. Petukhov, Heat transfer and friction in turbulent pipe flow with variable physical properties, in: Advances in Heat Transfer, Vol. 6, Elsevier, 1970, pp. 503–564, http://dx.doi.org/10.1016/S0065-2717(08)70153-9.
[32] P.K. Swamee, A.K. Jain, Explicit equations for pipe-flow problems, J. Hydraul. Div. 102 (5) (1976) 657–664, http://dx.doi.org/10.1061/JYCEAJ.0004542.
[33] W. Flaig, R. Mertz, J. Starflinger, Setup of the supercritical CO2 test facility "SCARLETT" for basic experimental investigations of a compact heat exchanger for an innovative decay heat removal system, J. Nucl. Eng. Radiat. Sci. 4 (031004) (2018) http://dx.doi.org/10.1115/1.4039595.
[34] S. Kakaç, R.K. Shah, W. Aung, Handbook of Single-Phase Convective Heat Transfer, J. Wiley and sons, New York Chichester Brisbane, 1987.
[35] I.L. Pioro, R.B. Duffey, Heat Transfer and Hydraulic Resistance at Supercritical Pressures in Power-Engineering Applications, ASME Press, New York, 2007.
[36] D.M. McEligot, C.W. Coon, H.C. Perkins, Relaminarization in tubes, Int. J. Heat Mass Transfer 13 (2) (1970) 431–433, http://dx.doi.org/10.1016/0017-9310(70)90118-3.
[37] M. Azarifar, M. Arik, J.-Y. Chang, Liquid cooling of data centers: A necessity facing challenges, Appl. Therm. Eng. 247 (2024) 123112, http://dx.doi.org/10.1016/j.applthermaleng.2024.123112.
[38] N. Bacchetta, J.-J. Blaising, E. Brondolin, M. Dam, D. Dannheim, K. Elsener, D. Hynds, P. Janot, A.M. Kolano, E. Leogrande, L. Linssen, A. Nürnberg, E.F. Perez, M. Petrič, P. Roloff, A. Sailer, N. Siegrist, O. Viazlo, G.G. Voutsinas, M.A. Weber, CLD – A Detector Concept for the FCC-ee, 2019, http://dx.doi.org/10.48550/arXiv.1911.12230, arXiv:1911.12230.